Water Research 285 (2025) 124152

Contents lists available at ScienceDirect

Water Research

journal homepage: www.elsevier.com/locate/watres

Contrast-Enhanced micro-computed tomography for 3D imaging of biofilms in opaque materials: Insights from water treatment plant sand filters

Laurenz Schröer [a,*], Tim Balcaen [b,c,d], Karel Folens [e], Nico Boon [e], Tim De Kock [f], Mandana Samari-Kermani [g], Greet Kerckhofs [b,c,h], Veerle Cnudde [a,g]

[a] PProGRess-UGCT, Department of Geology, Ghent University, Belgium
[b] Materials, and Civil Engineering (iMMC), Institute of Mechanics, UCLouvain, Belgium
[c] Institute of Experimental and Clinical Research (IREC), UCLouvain, Belgium
[d] Sustainable Chemistry of Molecules and Metals, Department of Chemistry, KU Leuven, Belgium
[e] Center for Microbial Ecology and Technology (CMET), Department of Biotechnology, Ghent University, Belgium
[f] Antwerp Cultural Heritage Sciences (ARCHES), University of Antwerp, Belgium
[g] Environmental hydrogeology, Department of Earth Sciences, Utrecht University, the Netherlands
[h] Prometheus, Division of Skeletal Tissue Engineering, Department of Materials Engineering, KU Leuven, Belgium

ARTICLE INFO

Keywords:
µCT
Drinking water
Porous media
Contrast-enhancing staining agents
Isotonic Lugol
Hf-WD 1:2 POM

ABSTRACT

Microorganisms form biofilms in various environments, including porous media, where they alter substrate properties and fluid flow. Visualizing biofilms in 3D within the pore system is essential to understand their effect. Micro-computed tomography (µCT) is a powerful technique to visualize the pore system, but biofilms are usually invisible due to low contrast with water. Contrast-enhancing staining agents (CESAs) can improve their visibility by changing the attenuation of the biofilm or water phase. Traditional CESAs such as $BaSO_4$, silver-coated microspheres or 1-chloronapthalene proved to be successful, but often stain the water phase and have drawbacks such as sedimentation or toxicity. After the successful use of isotonic Lugol and Hf-WD 1:2 POM on cyanobacteria at the surface, this study investigated the use of those CESAs to stain biofilms within opaque materials and, in particular, on biofilms colonizing field-derived sand filters of water treatment plants. Both CESAs increased the biofilms' visibility, including channels within the Hf-WD 1:2 POM stained biofilms and improved segmentation. Their visualization was consistent with Scanning Electron Microscopy (SEM). The CESAs quickly stained the biofilms, and their effect was stable. Isotonic Lugol enhanced the X-ray attenuation the most but might have caused shrinkage. The use of $BaSO_4$ solution, added for comparison and positive control, was complicated due to its fast precipitation. $BaSO_4$ was unable to visualize the isotonic Lugol-stained biofilms but corresponded with the Hf-WD 1:2 POM-stained biofilms. However, the stability and detail shown by isotonic Lugol and Hf-WD 1:2 POM make the latter two preferred. The study showed the potential of µCT and these CESAs for biofilm visualization and water research. Future research should apply these CESAs and focus on the CESA-biofilm interaction to understand the binding mechanisms and their effect on the structure.

1. Introduction

Microorganisms colonize along with the surface, the pores and cracks of materials, including rocks, sediments and soils. Within soils, bacteria are dominant with fungi, while in the deep subsurface, bacteria dominate with archaea (Bar-On et al., 2018; Fierer, 2017; Flemming and Wuertz, 2019). Almost all microorganisms are attached to the substrate, as between 20 % and 80 % would be part of a biofilm (Flemming and Wuertz, 2019; Konhauser, 2007). Biofilms within the pore network have a crucial influence. Biofilms actively participate in rock-water interactions. They affect elemental cycling and the chemistry of the substratum by, e.g., acid production and redox reactions that could induce mineral dissolution or precipitation (Ehrlich, 1999; Schröer et al., 2021). Their growth alters fluid transport, including flow paths and velocities, as the biofilms themselves or produced metabolites (e.g., calcium carbonate precipitation or gas production) can obstruct the pore space and induce bioclogging, reducing the hydraulic conductivity and permeability (Baveye et al., 1998; Carrel et al., 2018; Karimifard et al.,

* Corresponding author.
E-mail address: laurenz.schroer@ugent.be (L. Schröer).

https://doi.org/10.1016/j.watres.2025.124152
Received 30 October 2024; Received in revised form 27 June 2025; Accepted 2 July 2025
Available online 3 July 2025

2021; Schröer et al., 2022a). Furthermore, biofilms can change the geometry and topography of the surfaces and the wettability (Karimi et al., 2012; Schröer et al., 2022a) and the surface charge (Walker et al., 2004). The biofilms' location, extent, and composition depend on the physical and chemical properties of the porous medium and environmental conditions. It includes the pore structure in general, such as the porosity, pore size distribution, and surface roughness, but also the mineralogy, water content, pH, temperature, etc. (Miller et al., 2012; Schröer et al., 2021).

Microorganisms and biofilms can positively impact numerous economic and environmental processes. They can be used to bioremediate groundwater (Coombs et al., 2010; Meckenstock et al., 2015), clean wastewater (di Biase et al., 2019), produce drinking water (Bai et al., 2023), stop the spreading of pollution (Kalin, 2004) or carbon dioxide sequestration (Ebigbo et al., 2010). Furthermore, they can contribute to protecting and restoring building materials (De Muynck et al., 2010; Schröer et al., 2022a, 2021). However, they can also have a negative impact as some microorganisms can induce biodeterioration of building materials (Schröer et al., 2022b, 2021, 2020). Some bacteria could even be dangerous when they spread, e.g., in groundwater (Pedley and Howard, 1997), or biofilm formation in catheters can cause infections (Pelling et al., 2019).

Concerning the impact biofilms can have on porous materials, it is essential to study their occurrence and understand their influence on the pore system and how the pore system affects the biofilms. There are numerous tools to visualize biofilms at the surface, such as optical microscopy, scanning electron microscopy (SEM), cryo-SEM, environmental SEM or confocal laser scanning microscopy (Azeredo et al., 2017). Visualizing biofilms inside opaque porous media is much more challenging. Hence, multiple theoretical models were developed to describe biofilm growth and their effect on fluid transport (e.g., (Pintelon et al., 2009; Qin and Hassanizadeh, 2015; Schulz and Knabner, 2017). However, empirical evidence is necessary to validate these models. Most studies were limited to one or two dimensions. 1D flow fields were studied using column experiments (Vandevivere and Baveye, 1992), while 2D flow fields were studied by developing microfluidic devices (Hassanpourfard et al., 2016; Singh et al., 2017). 1- and 2D experiments simplify reality, and current research should study biofilms in 3D on natural heterogeneous materials.

Only a few methods can visualize biofilms within porous media in 3D. These include optical coherence tomography (OCT) and Magnetic Resonance Imaging (MRI). However, these techniques have limitations as OCT is limited to transparent materials (Wagner and Horn, 2017) and MRI has long acquisition times, in the order of several hours, and a limited resolution of around tens of micrometers (Caizán-Juanarena et al., 2019). Another possibility is micro-computed tomography (μCT), which can non-destructively visualize non-destructively opaque materials in 3D and is suited to study pore-scale processes. Depending on the settings, it can retrieve micrometer resolutions in a reasonable time (i.e., minutes or even seconds) (Bultreys et al., 2016; Cnudde and Boone, 2013; Withers et al., 2021).

The main challenge for absorption μCT in biofilm research is the lack of contrast between the biofilm and the surrounding water phase. Biofilms contain about 97 % water (Flemming et al., 2016) and are composed of light elements such as C, H, O, N, S and P. It results in similar X-ray attenuation between the biofilm and water phase. Contrast-enhancing staining agents (CESAs) could be applied to overcome this issue. CESAs are compounds that should be able to interact with biological material and contain heavy metals in their structure that can attenuate X-rays to induce contrast. Ideally, they also need to be soluble in the preferred solvent, not irreversible change the microstructure of the organic compound, have varying affinities towards organic materials, have short staining times, be non-toxic and easy to synthesize or commercially available (Balcaen et al., 2025). Multiple CESAs proved to be successful in visualizing biofilms, including barium sulfate ($BaSO_4$) (Davit et al., 2011), silver-coated microspheres (Iltis et al., 2011), iron sulfate ($Fe^{II}SO_4{\cdot}7H_2O$) (Carrel et al., 2017), 1-chloronaphtalene (Ivankovic et al., 2016; Rolland du Roscoat et al., 2014), iohexol (Tang et al., 2023) or Alcian blue (Zhang et al., 2018). However, several have drawbacks related to, e.g., toxicity (e.g., 1-chloronaphtalene), the fact that several do not stain the biofilm but the water phase with particles that can sediment and influence the fluid's viscosity (e.g., barium sulfate and silver-coated microspheres), ease of use (e.g., iron sulfate), etc. Moreover, research is limited, as none of the aforementioned CESAs are routinely used to visualize biofilms.

Therefore new easy to use and stable CESAs are necessary. In previous research by Schröer et al. (2024), isotonic Lugol's iodine solution (referred to as isotonic Lugol) and Hf-WD 1:2 POM (1:2 hafnium (IV)-substituted Wells-Dawson polyoxometalate $K_{16}[Hf(\alpha_2\text{-}P_2W_{17}O_{61})_2]{\cdot}19H_2O$) successfully enhanced the contrast of cyanobacterial biofilms colonizing sandstone, allowing even the visualization of internal features and/or filaments of the cyanobacterial biofilm. Within this study, the use of isotonic Lugol and Hf-WD 1:2 POM will be further explored to image the biofilm's location. It is not the goal to visualize the biofilm growth within the same sample over time. μCT is non-destructive, but these stains are expected to kill and inhibit further biofilm growth, and X-ray radiation can have a sterilizing effect. If biofilm growth needs to be studied over a longer time in the same sample, other CESAs could be further explored (e.g. iron sulfate (Carrel et al., 2017)).

Isotonic Lugol and Hf-WD 1:2 POM will be evaluated on biofilms colonizing the pore space of field-derived sand filters used in water treatment plants. This research stands out by visualizing biofilms in opaque materials that consist of heterotrophic bacteria. Biofilms play a crucial role in such systems, particularly in slow sand filtration, on which a bioactive layer is formed called the Schmutzdecke that enhances microbial degradation of organic matter and facilitates pathogen removal through predation, competition, and adsorption, thereby improving filtration efficiency (Dullemont et al., 2006; Maiyo et al., 2023). As biofilms develop, they alter pore and grain size distribution, creating preferential flow paths that affect fluid dynamics and particle transport within the media. Excessive biofilm growth can clog pore spaces, reduce flow rates, and increase hydraulic resistance, necessitating Schmutzdecke removal or backwashing, which raises operational costs and downtime (Samari-Kermani et al., 2024). In slow sand filters, μCT could provide a non-destructive means to determine the location of the biofilm, grain and pore size distribution, biofilm penetration depth, and identify clogged pore spaces and biofilm structures. All these insights are critical for understanding removal mechanisms and supporting macro-scale experimental observations. However, the biofilm needs to be visible. Therefore, samples from slow sand filters will be used to determine if these CESAs can visualize biofilms within opaque materials and to demonstrate their practical use in the field. Numerous measurements on triplicates will be performed to assess the stability of the CESAs, determine the optimal staining time, and evaluate whether washing to remove unattached CESAs can improve the results. These results will be verified by $BaSO_4$ particles (according to Davit et al., 2011) and Scanning Electron Microscopy (SEM).

2. Materials and methods

2.1. Materials

The CESAs were chosen based on previous work on visualizing cyanobacterial biofilms colonizing sandstone by Schröer et al. (2024). In that study, five different CESAs: Isotonic Lugol, Hexabrix®, Hf-WD 1:2 POM, Mono-WD POM and CA4+ were evaluated. They contain all heavy elements, can be dissolved in water and represent a wide variety, including both organic and inorganic molecules with positive and negative charges and a large variety in molecule sizes (Balcaen et al., 2025). They are known to enhance the contrast of different tissues, which have similar primary constituents (Woodard and White, 1986 as

biofilms. Isotonic Lugol and Hf-WD 1:2 POM were the most successful and selected for this study. Isotonic Lugol was used to stain respectively muscle tissue (Jeffery et al., 2011) and ligaments (Balint et al., 2016). Moreover, iodine species are known to interact with a large number of biomolecules, such as proteins (Early et al., 2020), lipids (Palumbo and Zullo, 1987) and polysaccharides (Moulay, 2013). Lugol's iodine is an aqueous solution of iodine and potassium iodide, which are in equilibrium with triiodide (and other iodine species to a lesser extent). This multifunctional stain can increase the attenuation of lipids by dissolving hydrophobic iodine in lipid pockets and can subsequently react with unsaturated double bonds to form reversible covalent bonds. Moreover, it can interact with proteins, and more specifically, activated aromatic amino acids, by forming a stronger covalent bond. Lastly, all iodine species can interact with biomolecules through non-covalent interactions (Balcaen et al., 2025; Early et al., 2020; Gignac and Kley, 2014). Hf-WD 1:2 POM successfully stained murine long bones and kidneys (de Bournonville et al., 2020) and is known to interact strongly with proteins. POMs can interact with proteins by charge-charge, hydrogen bonding and van der Waals noncovalent interactions, as well as coordinate and covalent binding (Salazar Marcano et al., 2023).

Isotonic Lugol solution (155.99 mM KI and 51.01 mM I_2) was prepared by dissolving 12.948 g KI and 6.474 g I_2 in 500 mL MilliQ water. It was diluted with PBS (10 mM) at a 1:1 ratio. A solution isotonic towards biological tissues was used to minimize the adverse effects of Lugol's iodine on the biofilms (de Bournonville et al., 2019). Hf-WD 1:2 POM was prepared by dissolving 35 g/L Hf-WD 1:2 POM in a PBS (10 mM) solution (de Bournonville et al., 2020). The Hf-WD 1:2 POM was synthesized in-house according to literature procedures (Ginsberg, 1990; Kato et al., 2006). Purity was confirmed by 31P NMR (calibration of the spectrum with an 85 V % H_3PO_4 solution external reference and comparison of NMR chemical shifts with literature). The $BaSO_4$ (Guerbet) solution was used in analogy to the experiments of Davit et al. (2011). The solution had an initial concentration of 1 mg/mL $BaSO_4$ but was diluted in PBS to reach a final concentration of 0.33 mg/mL. It aimed to increase the attenuation of the water phase and acted as a positive control.

The experiments were performed on sand samples from the top of filters of water treatment plants in The Netherlands. Four samples were used for isotonic Lugol (Sample $IL_1 - IL_3 + IL_{SEM}$), and four to test Hf-WD 1:2 POM (Sample $Hf_1 - Hf_3 + Hf_{sem}$), of which three samples were for μCT and one for SEM. The experiment was performed in triplicate. The filters consist of 1 to 2 m layers of sand, with on top a 3 cm deep bioreactive layer (Schmutzdecke), which was examined for these experiments.

The IL samples were taken from slow sand filter 5B of Monster production site, Dunea Water Company in The Netherlands. This filter had an average grain diameter (d50) of 0.66 mm, and the flow rate was 0.49 cm/h. At the time of sampling, the filter had not been scraped in five years. Hf samples were collected from slow sand filter 2 at Groningen Water Company in The Netherlands. This filter had a sand length of 100 cm, with around 2 m of supernatant above, and the flow rate was 15–20 cm/h. Both IL and Hf samples were taken a few hours after draining the filters, and the supernatant water was below the sand bed for the scraping.

Periodically, the top centimeters of the slow sand filters need to be removed due to the building up of head loss, a measure of clogging by the biofilm. At this time, the filters could be sampled. The intact samples were then kept at -20 °C until imaging. Although this might affect the microbial community of the samples, the biofilm can still stay on the grains. These samples were chosen as they were field-derived and extensive biofilms should be present. Due to a limited number of samples, both CESAs could not be tested on material from the same site. However, this should not be a problem, as research showed that diverse and complex microbial communities occur within slow sand filters (Haig et al., 2014). The microbial community of the Hf-WD 1:2 POM stained samples is unknown, but the community of another sample of slow sand filter 5B that was also used to test isotonic Lugol was studied by Bai et al. (2023).

2.2. Scanning electron microscopy (SEM)

Biofilm and sand grains were taken from one unstained replicate sample (sample IL_{SEM} and Hf_{SEM}) to visualize the biofilms using SEM as a ground truth. The biofilms were fixed in 2.5 % glutaraldehyde in PBS (10 mM) to avoid drying out the biofilm and destroying the cells by the vacuum of the SEM. Hereafter, they were dehydrated by an ethanol dehydration series of 50, 75, 90 and 3 × 100 %. The samples were imaged on the MIRA 3 TESCAN SEM system equipped with a Field Emission Gun (FEG) at the Geology Department of Ghent University. Back Scattered Electron Images (BSE) were taken to visualize the biofilms. Line profiles and point measurements using energy-dispersive X-ray spectroscopy (EDS (EDAX)) were taken to provide chemical information.

2.3. Experimental procedure

Each replicate was used to test the different CESAs. The CESAs were added to and removed from the sand samples using a simple flow setup, shown in Fig. 1. The samples were preserved in syringes that were sealed at the bottom. Solutions were added by attaching a tube at the bottom of the sample connected to the syringe pump. The solution that percolated through the samples could be drained by an outlet line if we used a flow cell, but here it was removed manually from the top by a pipette. After adding a solution, the samples were detached from the flow setup and sealed at the bottom with a gum that allowed attaching them later again to the syringe pump.

The experiment lasted five days per set of triplicates, during which PBS, CESA solution, and $BaSO_4$ were added, and six μCT scans were taken. During these five days, all samples were stored at room temperature. The scans of the triplicates were done on the same day but could not be done simultaneously. The same sample order was maintained to scan the samples relatively at a similar time.

Table 1 describes the detailed procedure. On Day 1, the biofilms were defrosted and rehydrated using a PBS (10 mM) solution. After 1.5 and 2 h, a first μCT scan of every sample was taken as (IL_x/Hf_x_Blank), with x as the sample number ranging from numbers 1 to 3 for every sample. Hereafter, the CESA solution was added. After around 18 – 21 h (depending on the sample), on Day 2, μCT scans were taken (IL_x/Hf_x_CESA), just as around 24 h later, on Day 3 (IL_x/Hf_x_CESA+1d). On Day 4, the samples were washed with PBS to remove the unattached contrast agent. A series of two μCT scans were taken: one immediately after washing with PBS (IL_x/Hf_x_Washed) and one around 24 h later (ILx/Hfx_Washed+1d).

500 μL subsamples of the isotonic Lugol were taken to measure the pH since this can provide information on the occurrence of specific chemical reactions. pH measurements were performed using a FiveEasy pH meter F20 (Mettler Toledo) with pH microelectrodes (InLab® Micro). The subsamples were taken after adding the CESA on Days 1, 2 and 3, and of the PBS solution around 24 h after removal of the unattached CESA on Day 4.

Finally, a 0.33 mg/mL $BaSO_4$ solution (Guerbet) was pumped through the sample. Immediately after adding $BaSO_4$, the samples were scanned one last time (IL_x/Hf_x_$BaSO_4$).

2.4. Acquisition of CT images and reconstruction

Only the top section, including the first millimeters of the sand filter and some supernatant, was scanned, as this zone is the Schmutzdecke with the highest biofilm concentration. All scans were performed using the CoreTOM scanner (Tescan XRE), at the Centre for X-ray Tomography (UGCT) at Ghent University, using binning 2. They were scanned at 90 kV, 15 W and a voxel size of 12.5 μm in X, Y and Z. 2142 projections

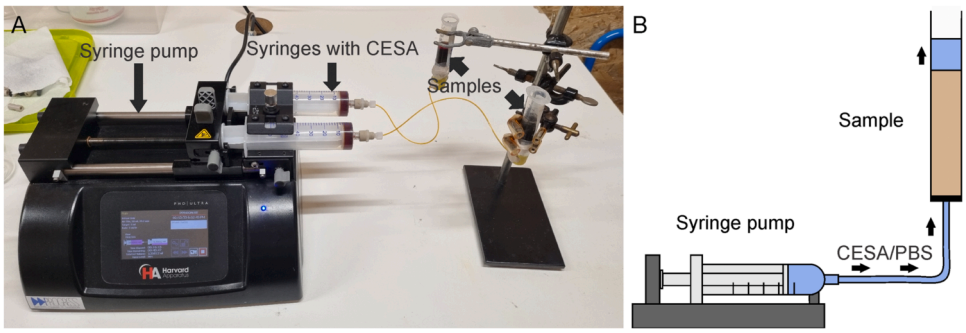

Fig. 1. (A) Picture of the setup, showing the syringe pump injecting isotonic Lugol in the sand samples containing the biofilms. (B) Schematic diagram of the injection of either CESA or PBS through the sample using a syringe pump.

Table 1
Procedure of the experiment on the different days and the scans that were taken, with their corresponding name between brackets with x corresponding to the sample number ranging from 1 to 3.

Day	Procedure
Day 1	1. Rehydrate the sample by pumping PBS at 5 mL/h
	2. Take the first μCT scan (IL_x/Hf_x_Blank)
	3. Inject CESA, either isotonic Lugol or Hf-WD 1:2 POM, at 5 mL/h for 2 h
Day 2	4. Take μCT scan while submerged in the CESA (IL_x/Hf_x_CESA)
Day 3	5. Take μCT scan while submerged in the CESA (IL_x/Hf_x_CESA+1d)
Day 4	6. Remove unattached contrast agent by pumping PBS at 10 mL/h for 75 min
	7. Take μCT scan (IL_x/Hf_x_Washed)
Day 5	8. Take μCT scan (IL_x/Hf_x_Washed+1d)
	9. Pump $BaSO_4$ in the samples at 2 mL/h until fully immersed
	10. Take μCT scan (IL_x/Hf_x_$BaSO_4$)

were taken at an exposure time of 950 ms/projections. Furthermore, two averages of each projection were taken to improve image quality (except for IL_x_Blank, where only one average was taken). Low-energy X-rays were removed using a 1 mm Al filter to reduce beam hardening. One scan took about 75 min. The projection data were reconstructed using the Panthera software (Tescan XRE), where a correction for beam hardening and ring filters was applied. One exception was the last scans after the addition of $BaSO_4$. Preliminary testing showed that the $BaSO_4$ particles rapidly sedimented, and therefore, the scan duration was reduced to about 18 min. The 1 mm Al filter was kept, but the voltage was increased to 120 kV and the power to 17.5 W, while the exposure time decreased to 500 ms/projection, and only 1542 projections were retrieved, using one average. The final voxel size was 17.5 μm in X, Y and Z. The reconstruction parameters were identical between the triplicates to allow comparison.

2.5. Image analysis

Image analyses were conducted using Fiji and Avizo (Thermo Fisher Scientific). At first, the different phases (biofilm, sand, liquid (PBS or CESA), gas) were segmented in Fiji using Weka 3D segmentation (Arganda-Carreras et al., 2017). Weka segmentation was necessary as the loose sand grains moved between the scans, making differential segmentation unfeasible. Furthermore, the complex nature of the sand grains, with impurities, made simple thresholding very challenging.

The training dataset consisted of a small volume of 500 × 500 × 300 voxels, in which a small number of annotations were made for the different phases. Segmentation results were obtained using an iterative approach with the Weka training features: texture (mean, variance), structures, and edges (canny edge detection). After the successful segmentation of the training datasets, this was used to automatically segment the whole μCT scan and the other replicates. It was performed using a tiling algorithm to reduce the memory requirements (Arganda-Carreras, 2018). Due to the different nature of the Hf and IL samples and the liquids (PBS or CESA), six training datasets were made. Three for each triplicate. One of each sample before adding the CESA (IL_x/Hf_x_Blank), one of each sample after adding the CESA (IL_x/Hf_x_CESA(+1d)), and one after washing the samples with PBS (IL_x/Hf_x_Washed(+1d)).

The rest of the analyses were performed using Avizo. At first, the internal part of the syringe, excluding the top and bottom slices, outer plastic wall and outer air, was used as a mask over the Weka segmented data. In the next phase, the average grey values and their standard deviation were determined for each phase, with their volume fraction, by using the global analysis tool. Grey values were transformed to attenuation coefficients by the slope and offset of the reconstructed images.

No Weka segmentation and analyses were performed after adding the $BaSO_4$ particles.

3. Results and discussions

3.1. Scanning-Electron microscopy (SEM)

SEM was performed to confirm the presence and characterize the biofilms. The BSE images indicated the sand grains and a disorganized phase identified as the biofilm (Fig. 2A-D). IL_{SEM} contained biofilms that mainly covered discrete parts of the grains (Fig. 2A). More biofilm was visible in Hf_{SEM}, where several particles consisted solely of biofilm (Fig. 2B), which was also more porous compared to the one of IL_{SEM}.

Elemental analyses by EDS should be interpreted with care, certainly when only a low number of counts were acquired. EDS detected phosphor and/or sulfur in the amorphous mass identified as biofilms. This is illustrated in Figs. 2E and 2F, where two line profiles show the elemental distribution along the grain/biofilm interface. Furthermore, higher concentrations of iron and/or manganese were found, just as calcium, phosphor, silica, aluminum and sodium. These could originate from the water that percolated through the sand filters.

Aluminum was not always present but was determined along some line profiles (Fig. 2E, F). Aluminum could indicate the presence of clays, which could interfere with the CESAs. Iodide could weakly interact with clays and may concentrate in the area around the clay particle and within the interlayer space (Miller et al., 2015). The interaction between Hf-WD 1:2 POM and clays has not been studied in detail. However, the low aluminum concentrations and the absence of clay-shaped minerals assumed that even if clays were present, their effect was limited.

3.2. Micro-computed tomography

After the identification of the biofilms in between the sand grains, the influence of both CESAs: isotonic Lugol and Hf-WD 1:2 POM was assessed.

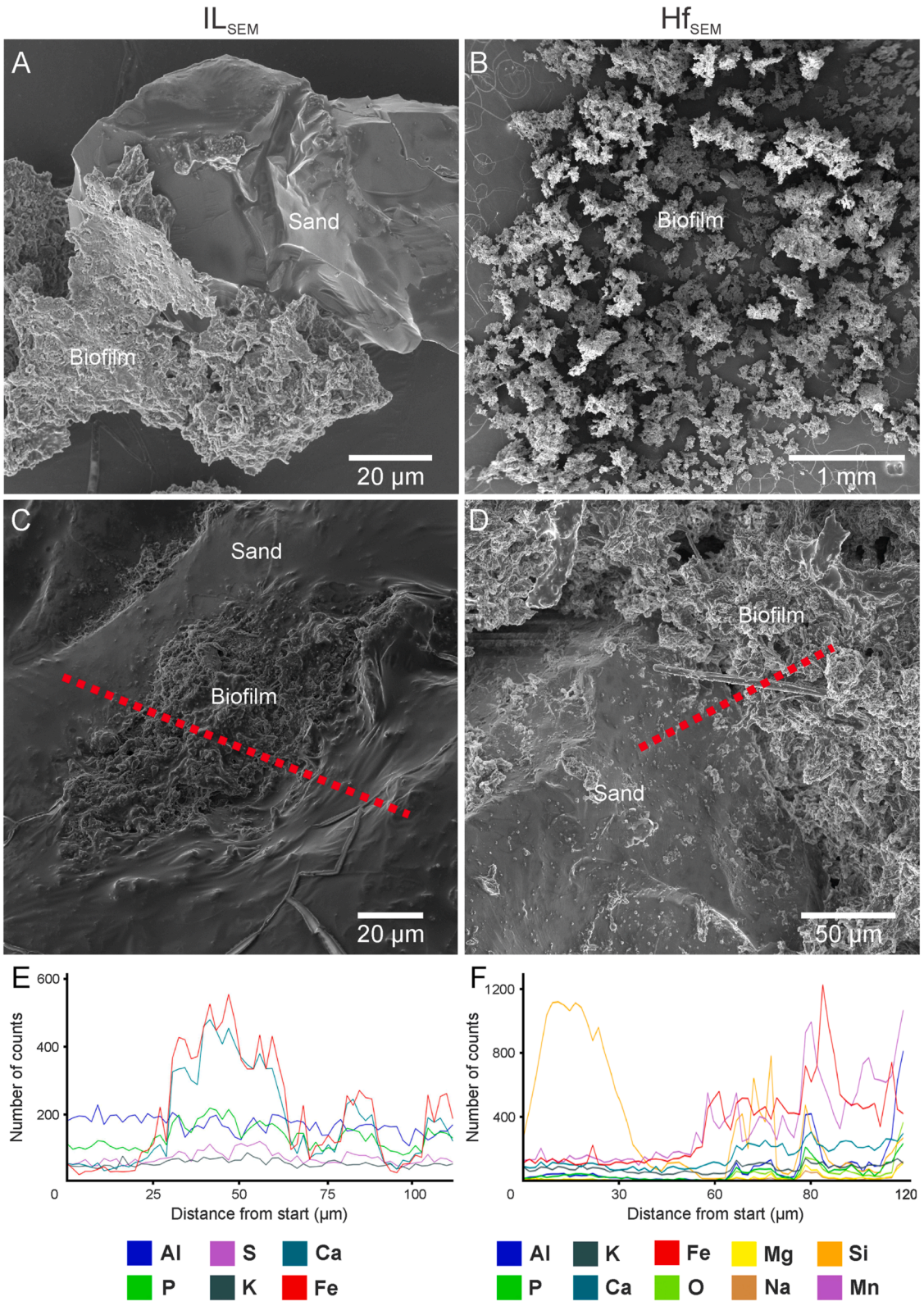

Fig. 2. (A-D) BSE image of sand particles and a highly disorganized phase interpreted as biofilms, taken from IL_{SEM} (A, C) and HF_{SEM} (B, D). (E-F) EDX line profiles showing the detection (in number of counts) of K-edges of elements from the left to the right along the red dotted line of respectively (C) for (E) and (D) for (F). The line profiles run from a zone with no visible biofilm on the left towards a zone covered by biofilms at the middle (E) or right (F). (E) shows the detection of Al, S, Ca, P, K and Fe along a partially covered sand grain of sample IL_{SEM}. The Si signal is not shown for visibility as its abundance was much higher (up to 5000 counts). (F) shows the detection of K edges of Al, P, K, Ca, Fe, O, Mg, Na, Si, and Mn along a partially covered sand grain of sample Hf_{SEM}.

3.2.1. Isotonic Lugol

Staining with isotonic Lugol had a substantial and consistent effect on the visualization of the biofilm phase (Fig. 3) among all triplicates. Within all the scans, three distinct phases were visible: Sand (highest grey value), liquid (medium grey value), and occasionally some trapped gas (lowest grey value) (Fig. 3A-E). The liquid phases consisted either of PBS or isotonic Lugol and included the liquid on top and the filled pores. Without applying the CESA, an extra phase was visible in the pore volume with a slightly higher grey value than the PBS solution (Fig. 3A). It was interpreted as biofilm as its shape corresponded to the SEM images (Fig 2A, C). It was surprising as a biofilm mainly consists of water (Flemming et al., 2016), resulting in a similar grey value. However, its relatively high attenuation was most likely linked to the presence of iron as detected by SEM-EDX (Fig. 2E).

After adding isotonic Lugol (Fig. 3B), the biofilm phase became better visible and obtained a higher attenuation coefficient, indicating an interaction between the CESA and the biofilm phase. The same result was observed after around another 24 h (Fig. 3C). Removing unattached iodine species by washing the samples with PBS reduced the attenuation of the biofilm phase and the liquid (Fig. 3D) while maintaining the contrast. It further indicates an interaction strong enough to withhold the iodine/iodide removal from the biofilm phase upon washing. No substantial changes occurred after around 24 h, as scans of IL_washed+1d were almost identical (Fig. 3E).

Finally, $BaSO_4$ particles were added to verify the location of the biofilm. However, before these scans, it was observed that the particles quickly settled, which made it necessary to take faster and noisier scans with a lower resolution. $BaSO_4$ failed to detect the biofilms' location (Fig. 3F). This was most likely caused by the high attenuation of the $BaSO_4$ that corresponded with the attenuation of the stained biofilm. Moreover, there was already precipitation visible of the $BaSO_4$, even though the scan lasted only 18 min.

Besides visualizing the biofilms within the pores, the main goal was to segment the biofilms, allowing further analyses. Segmentation was performed on all scans except after adding $BaSO_4$ using Weka. Weka segmentation could segment the sand grains, liquid, gas, and biofilm phases (Fig. 4B, D) by qualitative interpretation. Overall, the segmentation was successful, but it encountered some misclassifications, e.g., in identifying gas bubbles when the surrounding liquid consisted of PBS instead of the CESA, and nearly touching sand grains were often classified as one. However, it could distinguish most of the stained biofilms.

The average attenuation coefficients of each Weka segmented phase agreed with the qualitative observation described using Fig. 3. Fig. 4E provides an overview of the results in a graph; the numeric data is provided in Supplementary Information, Table S1. Initially (IL_Blank), the difference between the attenuation coefficient of the biofilm (0.69 ± 0.13) and the liquid (0.42 ± 0.11) was minor, while the sand was the most attenuating phase (1.38 ± 0.25). The attenuation coefficients of the sand phase varied, which was caused by the heterogeneity of the sand with several highly attenuating (parts of) grains. Adding isotonic Lugol (IL_CESA) increased the attenuation coefficient of the liquid phase (to 0.66 ± 0.11) and more than doubled the attenuation coefficient of the biofilms (to 1.65 ± 0.60). The high standard deviation suggests the complexity of the biofilms, with some parts attenuating more than the sand grains while others attenuating less. Almost no changes occurred after an extra 24 h (IL_CESA+1d), and washing (IL_Washed) lowered the

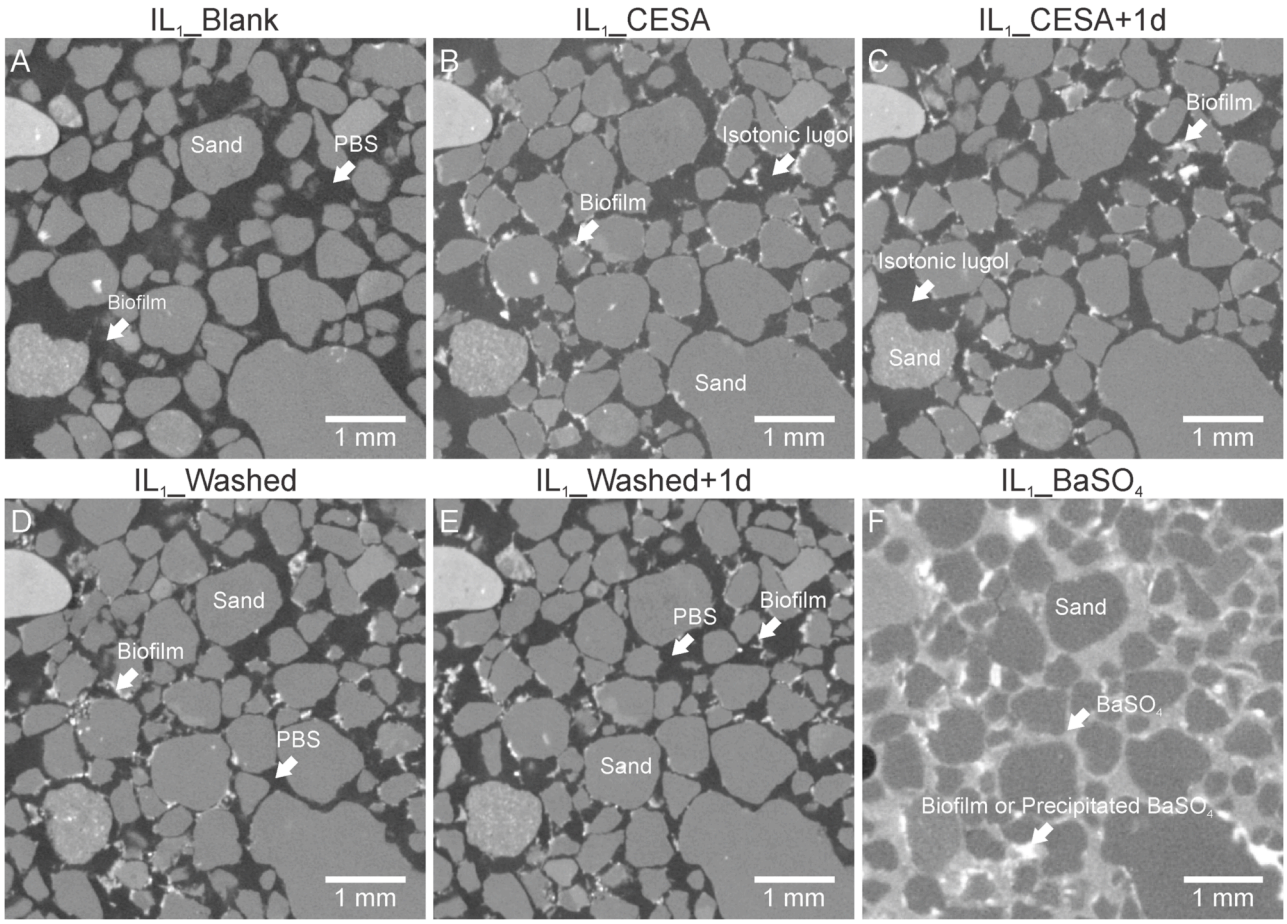

Fig. 3. (Parts of) horizontal µCT cross-sections of sample IL_1 through the upper part of the sand filter colonized by biofilms. The scans were taken (A) without adding a CESA, (B) one night (around 18 h) after adding isotonic Lugol, (C) after around another 24 h, (D) Immediately after washing with PBS, (E) after around 24 h, and (F) after adding $BaSO_4$ particles. The locations of the cross-sections in the images are not identical due to the internal movement of the sand grains between the scans.

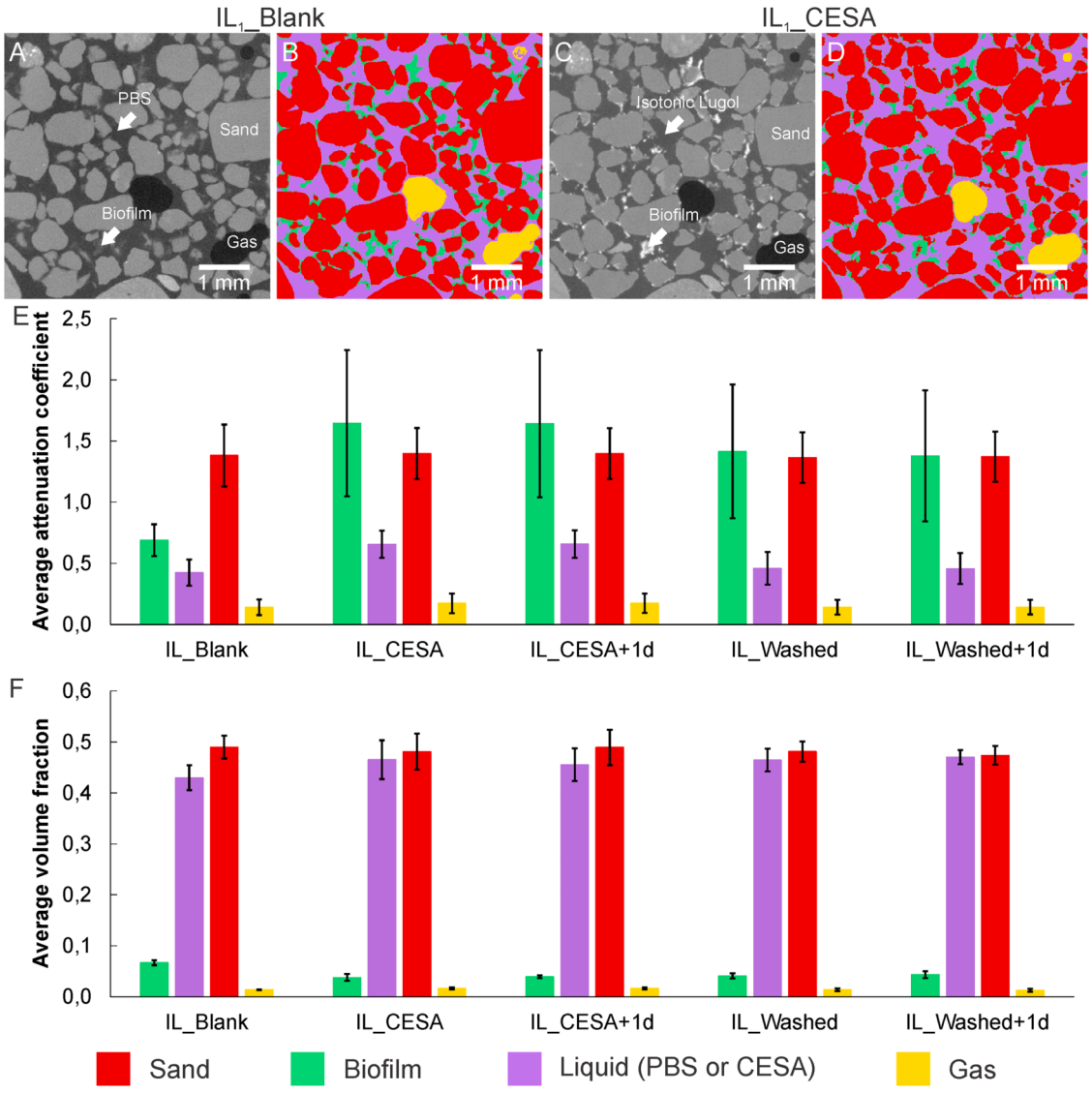

Fig. 4. Part of a cross-section of sample IL_1, before (A) and after staining with isotonic Lugol (C), with the corresponding Weka segmented image (B) and (D) with the sand phase in red, biofilm phase in green, surrounding liquid (either PBS or isotonic Lugol solution) in purple and gas in yellow. (E) Graph representing the average attenuation coefficients and the standard deviations within the difference phases ($n = 3$) of the biofilm, surrounding liquid (either PBS or isotonic Lugol), sand and gas phase. (F) Graph showing the average volume fraction of each phase with the standard deviation along the different scans ($n = 3$).

attenuation values of the biofilms (to 1.41 ± 0.55) and the liquid (to 0.46 ± 0.13) but did not have a substantial effect on the contrast. Furthermore, isotonic Lugol seemed to remain attached to the biofilm as no further considerable decrease in the attenuation coefficient of the biofilm was observed after around 24 h (IL_Washed+1d), where the average determined attenuation coefficient was 1.38 ± 0.53.

The robustness of the different training datasets and the Weka segmentation is illustrated by the volume fractions of the scans (Fig. 4E), of which all the numbers can be found in the Supplementary Information (Table S2). The data showed that the fraction of sand (between 0.490 ± 0.022 and 0.474 ± 0.018) remained relatively stable over the scans, as expected. It also agrees with the observations in Fig. 3 that the attenuation coefficient remained stable between the different scans. However, these values should be interpreted carefully as the grains moved between the scans, and the top surface could slightly differ. However, some changes occurred after the initial staining. As a striking result, Weka classified almost double the amount of unstained biofilm in IL_Blank compared to the stained biofilms of IL_CESA. The amount of classified biofilm dropped from 0.067 ± 0.005 to 0.038 ± 0.007. It resulted in a higher volume fraction of the liquid phase (from 0.430 ± 0.025 to 0.465 ± 0.038), while the sand fraction remained similar. The uncertainty of the correct segmentation of the unstained biofilm was higher, as the contrast was much lower. However, after qualitative interpretation and comparison with the SEM images, it was deemed acceptable and suggested that in some instances, advanced segmentation algorithms such as Weka can segment low-contrast biofilms. Lugol is known to induce shrinkage of muscle tissues between 25 % and 65 %, depending on the CESA concentration (Vickerton et al., 2013). Even an isotonic Lugol's iodine solution, optimized to avoid shrinkage caused by osmolality differences in mammalian biological tissue specimens, induced shrinkage in the past (Dawood et al., 2021; Maes et al., 2022). Its effect on biofilm is unknown, but a similar effect was assumed on cyanobacterial biofilms in which isotonic Lugol revealed filaments (Schröer et al., 2024). A decrease in pH can accompany shrinkage (Dawood et al., 2021; Maes et al., 2022). In our experiment, the measured pH values (Table S3 in supplementary information) fluctuated for the different samples between 7.17 and 7.45. They remained relatively stable during the experiment or even slightly increased for IL_2 from 7.22 to 7.41. However, the amount of biomass might have been too small to reduce the pH significantly, given that we work in a buffered system.

3.2.2. Hf-WD 1:2 POM

The effects of Hf-WD 1:2 POM were comparable to those for isotonic Lugol, but the attenuation enhancement was more moderate. There was also no considerable variation between the triplicates, illustrating the robustness of the CESA. The biofilm was very different compared to the IL samples, most likely as it originated from another treatment plant. Clumps of biofilm were present at the exterior above the sand surface and visible to the naked eye. The results are presented in Fig. 5, showing a part of a horizontal μCT cross-section during the different stages of the experiment.

Before adding the CESA, the sand and the liquid phase were again very well visible (Fig. 5A), together with some residual gas bubbles. The sand phase was heterogeneous, with some grains having a higher attenuation. Without CESA, the biofilm was again visible, with a slighter higher grey value than the surrounding liquid. It was mainly visible above the sand surface, while in between the grains, not much biofilm could be distinguished. The biofilm corresponded to the visual observation by the naked eye and the SEM images (Fig. 2B). The contrast was most likely induced by the presence of iron and/or manganese as detected by SEM-EDX (Fig. 2F). Adding Hf-WD 1:2 POM made the biofilm better visible above, but also in between the sand grains. It obtained an attenuation coefficient between the surrounding Hf-WD 1:2 POM solution and the sand grains. The biofilm phase was extensive and similar to the SEM data (Fig. 2B). No substantial changes occurred overnight after around 21 h (Fig. 5C), but some CESA precipitated and formed a layer above the sand. The amount of precipitation was variable and was the most pronounced in sample Hf_2 (Fig. 6A). The precipitate was visible on the μCT scan and as a white layer by the naked eye. The precipitation could be caused by the decomposition of the CESA or an interaction with one of the compounds. Hf-WD 1:2 POM reacted most likely with a compound of the biofilm: Mono-WD POM, which is very similar to Hf-WD 1:2 POM, is known to interact in the presence of calcium (de Bournonville et al., 2020). calcium was also detected on the biofilm by SEM-EDX. Interaction with the sand is less likely as it did not precipitate in previous experiments with Bentheim sandstone (Schröer et al., 2024). Washing the samples with PBS did not induce substantial changes. The only difference was that the liquid was replaced with PBS, became darker, and the biofilm seemed to become slightly darker as well (Fig. 5D). Washing could not remove the precipitated CESA, and the layer was even thicker (Fig. 6B). Everything remained stable after around 24 h, and no further changes were visible (Fig. 5E).

The Hf-WD 1:2 POM-stained biofilm was not only successfully visualized, but its internal structure featuring numerous channels, was also revealed (Fig. 5B-E). This finding highlights the potential of μCT and the CESAs for biofilm research. Although investigating the role of these channels in biofilm development and the sand filter performance is beyond the scope of this research, their importance is clear: they serve as conduits for oxygen transport for sustaining the biofilm (Verma et al., 2023; Wilking et al., 2013). These channels influence biofilm growth and consequently impact fluid transport within the porous media, in this case, the sand filter.

Adding $BaSO_4$ could confirm the presence of the biofilms (Fig. 5F). The biofilm on top could be easily distinguished as it remained dark as the particles did not enter. However, just as in the IL samples,

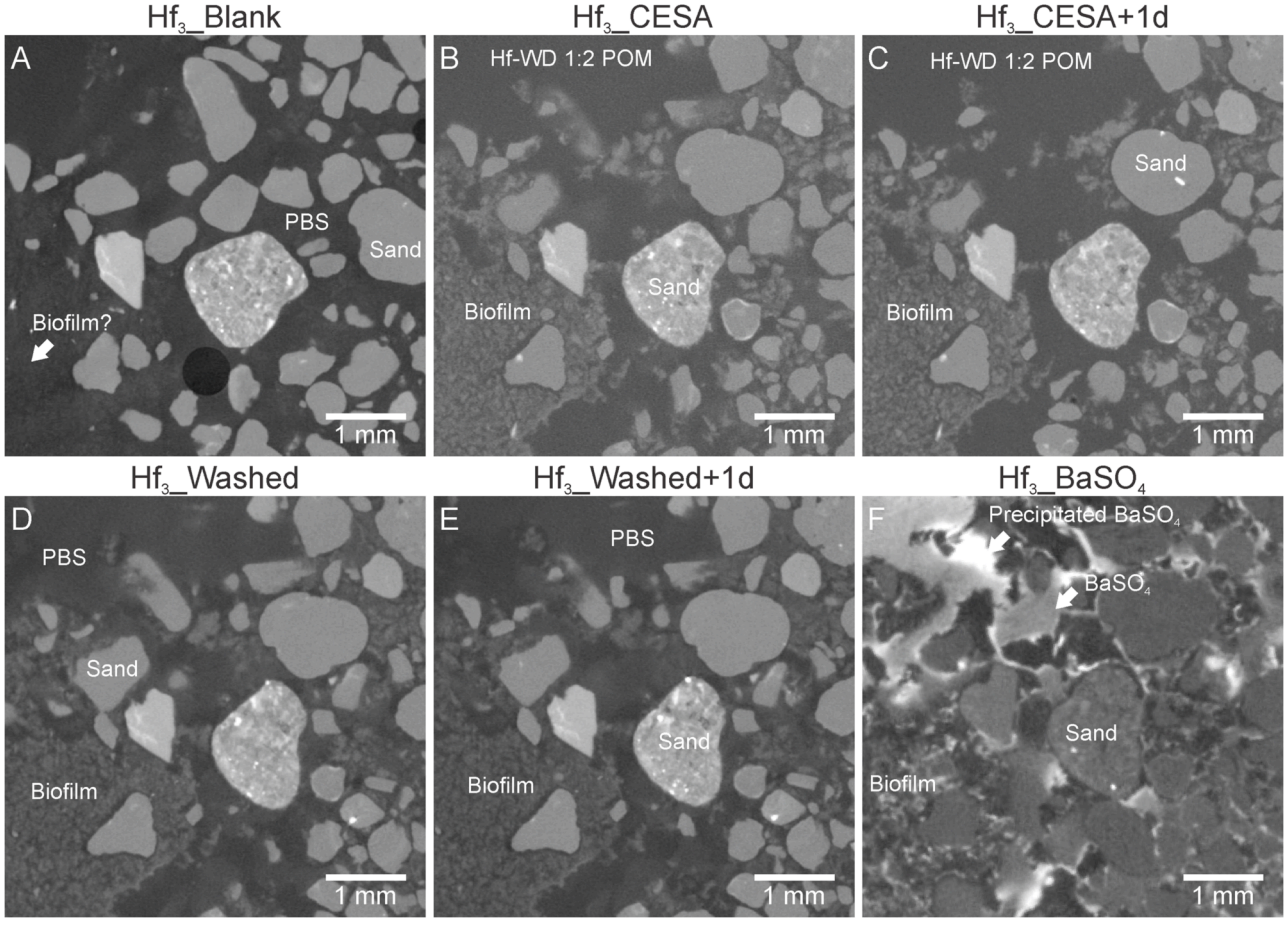

Fig. 5. (Parts of) Horizontal μCT cross-sections of sample Hf_3 through the sand filter colonized by biofilms. The cross-sections were taken near the top surface. The scans were taken (A) without adding a CESA, (B) One night (around 21 h after adding Hf-WD 1:2 POM, (C) after around another 24 h, (D) Immediately after washing with PBS, (E) after around 24 h and (F) after adding $BaSO_4$ particles. The locations of the cross-sections in the images are not identical due to the internal movement of the sand between the scans.

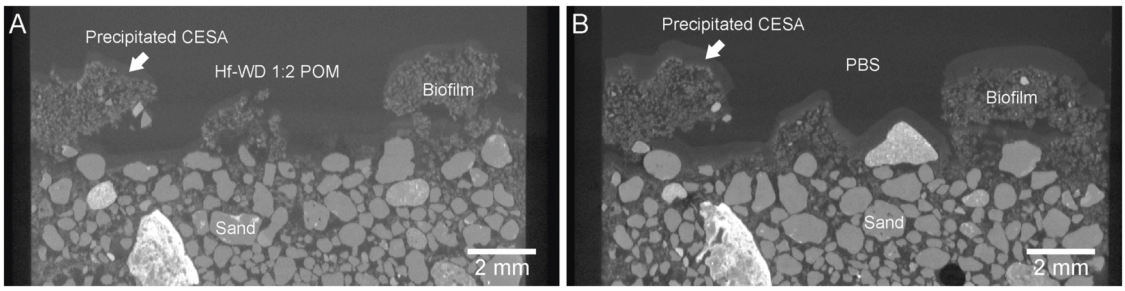

Fig. 6. Vertical cross-section through Hf_2 at (A) Day 3 (Hf_2_CESA+1d) and (B) after washing at Day 4 (Hf_2_Wash) showing the precipitated CESA on top of biofilm and sand grains.

precipitation was already visible. Details were much less resolved, as the channels in the biofilms were not well visible, and visualizing the biofilms inside the pores did not always work. Furthermore, the scans of Hf_1_$BaSO_4$ and Hf_2_$BaSO_4$ had a lot of motion artifacts caused by the downward movement of the sand in the syringe during scanning. The motion was assumed to be linked to pumping the viscous $BaSO_4$ solution through the sand just before the scan. Due to the bioclogging, the $BaSO_4$ solution could not easily percolate through the sample and pushed the sand upwards, which settled during scanning when no pumping occurred.

Qualitative observations after Weka segmentation showed that it could successfully segment the sand, liquid and gas phases (Fig. 7). It

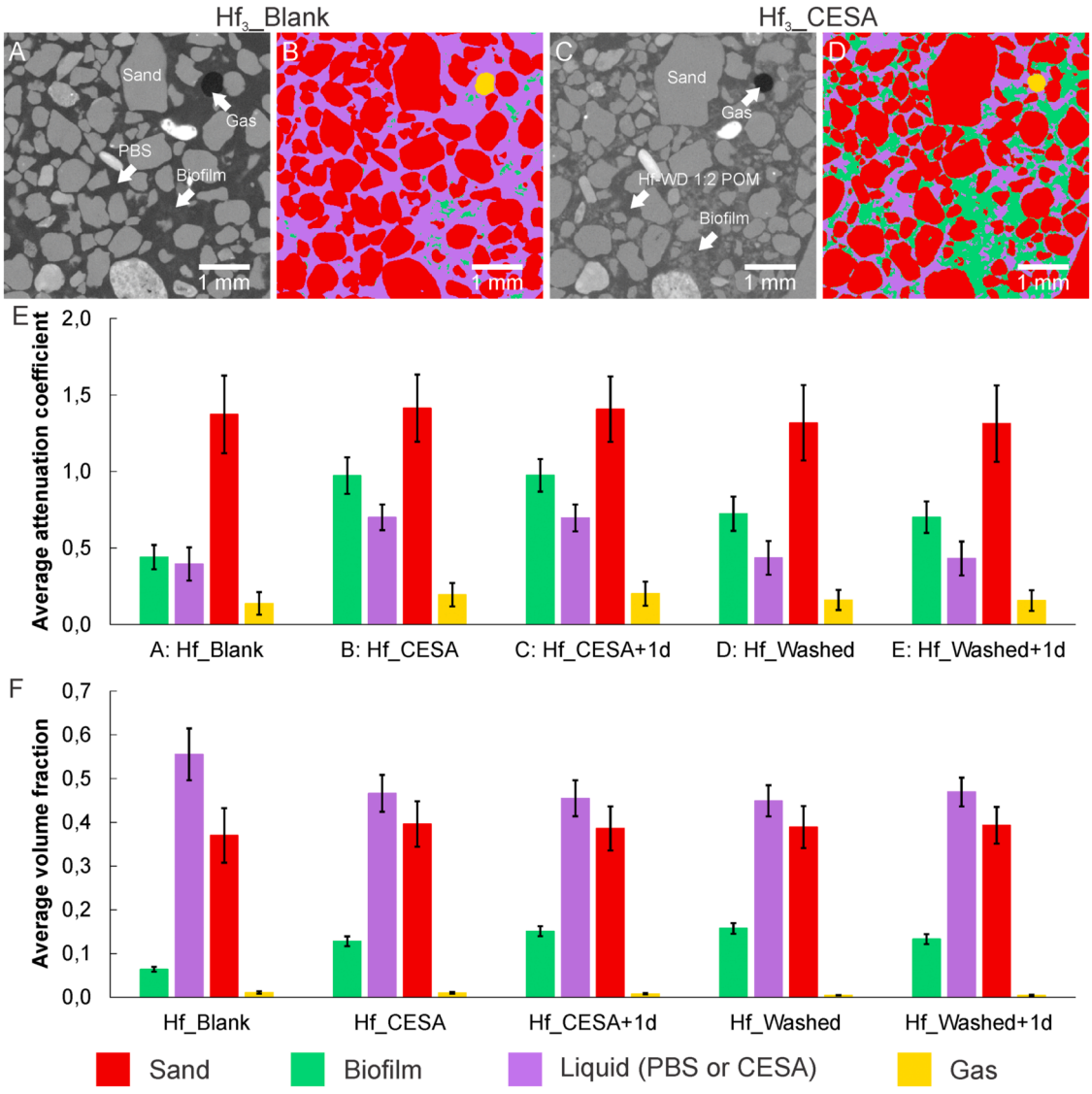

Fig. 7. Part of cross-sections of sample Hf_3, before (A) and after staining with Hf-WD 1:2 POM (C), with the corresponding Weka segmented image (B) and (D) with the sand phase in red, biofilm phase in green, surrounding liquid (either PBS or Hf-WD 1:2 POM) in purple and gas in yellow. (E) Graph representing the average attenuation coefficients and the standard deviations within the difference phases ($n = 3$) of the biofilm, surrounding liquid (either PBS or Hf-WD 1:2 POM), sand and gas phase. (F) Graph showing the average volume fraction of each phase with the standard deviation along the different scans ($n = 3$).

experienced similar errors as described for isotonic Lugol. However, this time, it could not fully segment the biofilm without CESA. The unstained biofilm had a lower attenuation coefficient compared to the IL samples, which could be related to lower Fe and/or Mn concentrations. Weka could assign some of the biofilm laying on top of the sand correctly, but the biofilm within the pores was not visible enough (Fig. 7B). More biofilm could be segmented with Weka after adding CESA (Fig. 7D). Qualitatively, the segmentation seemed successful, it was just unable to capture all the fine channels within the biofilm, which could be solved by further training and potentially higher resolution scans. Therefore, it most likely overestimated the amount of biofilm and underestimated the average attenuation coefficient of this phase, as shown by the graphs in Figs. 7E and 7F. The values and standard deviation can be found in the Supplementary Information, Tables S4 and S5.

The average attenuation coefficients of Fig. 7E showed a similar pattern as with isotonic Lugol. The part of the biofilm phase that could be assigned was initially (Hf_Blank) very similar to the surrounding PBS solution (0.44 ± 0.08 vs. 0.40 ± 0.11). Adding Hf-WD 1:2 POM (Hf_CESA) more than doubled the attenuation coefficient of the identified biofilm phase from 0.97 ± 0.12, and increased the attenuation coefficient of the solution to 0.70 ± 0.08. However, the contrast was enhanced significantly, and the attenuation coefficient of the biofilm remained below the one of the sand phase (1.41 ± 0.22). The effect of Hf-WD 1:2 POM in these samples was smaller compared to isotonic Lugol in IL_CESA, where an average attenuation coefficient of 1.65 ± 0.60 was obtained. No considerable differences were observed overnight, after around 24 h (Hf_CESA+1d), so it was assumed that CESA was quickly absorbed by the biofilm and remained stable afterwards. Even though parts of the CESA precipitated, it did not affect the segmentation. It is thus advised to scan rapidly after staining to avoid precipitation, but no major problems are expected if it is not possible. Washing the sand with PBS (Hf_Wash) reduced the attenuation coefficient of the biofilm (0.72 ± 0.11) and the liquid (0.44 ± 0.11) again, but the contrast remained similar. No relevant reduction in attenuation was observed after 24 h (Hf_Wash+1d).

The volume fractions of the sand phase (Fig. 7F and Supplementary Information Table S4), ranging between 0.370 ± 0.062 and 0.393 ± 0.042, were relatively stable during the experiment and similar to the observations in the IL samples. Comparing the fractions should also be done with caution, as the sand grains moved between the scans. A larger fraction was classified as liquid compared to the IL samples. More space above the sand surface was included, as large pieces of biofilms were present there. Furthermore, double the amount was classified as biofilm after adding the CESA. The amount of biofilm increased from 0.064 ± 0.005 in Hf_Blank to 0.128 ± 0.011 in Hf_CESA, being the main cause of the decrease in the fraction of the liquid from 0.555 ± 0.059 to 0.466 ± 0.042. It was linked to the biofilms within the pores that were invisible without adding Hf-WD 1:2 POM. There might be some overestimation due to Weka, which mostly classified the channels in the biofilm as biofilm or swelling that could occur after using Hf-WD 1:2 POM, as observed in the literature (Maes et al., 2022). After the addition of the CESAs, no important changes occurred in the volume fractions of the phases. These results confirmed the enhanced visualization of the biofilm after staining and the stability of the induced contrast.

4. Conclusions and future perspectives

After the successful visualization of cyanobacteria at the surface by isotonic Lugol and Hf-WD 1:2 POM (Schröer et al., 2024), this study examined their use to stain heterotrophic biofilms colonizing opaque porous media. Furthermore, it showcased their use and added value of μCT for water research by successfully applying this technique to field-derived sand filter samples. Applying isotonic Lugol and Hf-WD 1:2 POM was straightforward and performed fast and stable biofilm staining, even for Hf-WD 1:2 POM, where some precipitation occurred after two days. The stain duration, overnight, between 18 and 21 h, was sufficient, and no positive effect was determined by increasing this time. Most likely, the enhanced contrast was already obtained in the first hour (s). Furthermore, the study showed that washing the unattached CESA from the pore system is unnecessary to improve the contrast.

Both CESAs provide new opportunities for μCT to reveal biofilms in opaque materials, where classical methods such as optical and confocal laser scanning microscopy are limited. It will allow to directly visualize in 3D the effect of biofilms in opaque porous media, such as sand filters, rocks, catheters, etc., and can impact the hydrological, geological, industrial and even medical fields. They outperform the more traditional $BaSO_4$, showing more details and are more stable, avoiding compromises related to the scan time and the resulting quality and resolution. Furthermore, isotonic Lugol and Hf-WD 1:2 POM seemed not to affect the fluid properties and should not cause abrasion and shear detachment, which was observed by $BaSO_4$ in a former study (Carrel et al., 2017). The application of μCT is not limited to locating biofilms in 3D, as the Hf-WD 1:2 POM stained biofilm (and to a smaller extent by $BaSO_4$) revealed the structure of the biofilm with channels.

Isotonic Lugol and Hf-WD 1:2 POM appear to be non-specific based, based on both this and previous research on cyanobacterial biofilm (Schröer et al., 2024). However, despite being tested on different samples, their effects varied. Isotonic Lugol provided a greater enhancement in attenuation compared to Hf-WD 1:2 POM. Future research should focus on the interaction between the CESAs and the biofilm. Different CESAs could potentially be combined to stain distinct components of the biofilms. Additionally, more specific CESAs should be explored to selectively target particular parts of the biofilm. The amount of shrinkage by isotonic Lugol and potential swelling by Hf-WD 1:2 POM (Maes et al., 2022) should be investigated in detail, as it will hinder the volume estimation of biofilms in porous media. It could be done by visualizing biofilms at an outer surface with other microscopic techniques, such as confocal microscopy, before and after staining. Moreover, the applicability of μCT to visualize the structure of biofilms should be explored as it adds a third dimension to biofilm research. Therefore, the interaction of CESAs and biofilm should be known. It is also recommended to enhance the resolution (e.g. by a smaller sample size) to explore which details in the biofilm's structure can be revealed. The resolution in lab-based μCT systems is limited to a few hundred nm and for many systems in the μm range. Therefore, synchrotron experiments might be necessary. Furthermore, the interaction with materials, such as clays, should be investigated as well to confirm if these CESAs could be used on materials, such as soils, as the CESA could potentially stain these materials as well.

Future research should also apply these CESAs in the field to answer scientific questions and make μCT a more standard technique to study biofilms and their effects. It includes water research and water treatment to assess the universality of the technique even more within these samples and also in other fields such as geology, cultural heritage, engineering, etc. Future research could also include a fourth dimension by performing fast dynamic μCT experiments (e.g. to image how biofilms in porous media affect fluid flow in real-time).

CRediT authorship contribution statement

Laurenz Schröer: Writing – review & editing, Writing – original draft, Visualization, Validation, Software, Methodology, Investigation, Formal analysis, Data curation, Conceptualization. **Tim Balcaen:** Writing – review & editing, Writing – original draft, Validation, Methodology, Investigation, Conceptualization. **Karel Folens:** Writing – review & editing, Writing – original draft, Investigation. **Nico Boon:** Writing – review & editing, Writing – original draft, Supervision, Resources, Methodology, Funding acquisition, Conceptualization. **Tim De Kock:** Writing – review & editing, Writing – original draft, Supervision, Resources, Methodology, Funding acquisition, Conceptualization. **Mandana Samari-Kermani:** Writing – review & editing, Writing – original draft, Resources. **Greet Kerckhofs:** Writing – review & editing,

Writing – original draft, Methodology, Conceptualization. **Veerle Cnudde:** Writing – review & editing, Writing – original draft, Supervision, Resources, Project administration, Methodology, Funding acquisition, Conceptualization.

Declaration of competing interest

The authors declare that they have no known competing financial interests or personal relationships that could have appeared to influence the work reported in this paper.

Acknowledgements

The authors acknowledge the Research Foundation – Flanders (Fonds Wetenschappelijk Onderzoek, FWO) for funding the PhD fellowship of Laurenz Schröer (Research Grants No. 11D4518N, 11D4520N) and for the support for Tim Balcaen and Greet Kerckhofs (G088218N) as well as the FWO infrastructure grants I002720N and I013118N. This project has received funding from the Dutch Research Council (NWO) through the BugControl project (project number VI.C.202.074) of the NWO Talent program and from the EXCITE network, part of the European Union's Horizon 2020 research and innovation program under grant agreement No 101005611. The Ghent University Special Research Fund (BOF-UGent) is acknowledged for their support to the UGent Core facility UGCT (BOF.COR.2022.0008), for providing funding to Karel Folens (BOF.PDO.2020.020) and the Industrial Research Fund (IOF), project FaCT F2021/IOF-Equip/021 to fund the CoreTOM system. The Laboratory of Organic Synthesis of Prof. Wim De Borggraeve is thanked for providing the CESAs. We are grateful for the funding of Tim Balcaen from Le Fonds de la Recherche Scientifique (FNRS) for the FRIA grant 40008717 and thankful for the Action de Recherche Concertée (ARC 19/24–097) - Fédération Wallonie-Bruxelles. Furthermore, we gratefully acknowledge Dunea and Groningen water companies in The Netherlands for granting access to sampling sites, with special thanks to Brent Pieterse and Inan Duran for their invaluable support in facilitating sample collection. We also extend our gratitude to Dr. Amir Raoof for his scientific and technical expertise in designing and constructing the sampler, which enabled intact sample collection. At last, we want to thank our colleagues at UGCT and PProGRess, including Prof. Matthieu Boone, Dr. Chandra Widyananda Winardhi and Iván Josipovic, for their help and advice.

Supplementary materials

Supplementary material associated with this article can be found, in the online version, at doi:10.1016/j.watres.2025.124152.

Data availability

All reconstructed μCT scans are available at the Yoda data repository of Utrecht University and accessible through: https://doi.org/10.24416/UU01-13TL1V.

References

Arganda-Carreras, I., 2018. Weka Segmentation tiling Script [WWW Document]. Scientific Community Image Forum.

Arganda-Carreras, I., Kaynig, V., Rueden, C., Eliceiri, K.W., Schindelin, J., Cardona, A., Seung, H.S., 2017. Trainable Weka Segmentation: a machine learning tool for microscopy pixel classification. Bioinformatics 33, 2424–2426. https://doi.org/10.1093/BIOINFORMATICS/BTX180.

Azeredo, J., Azevedo, N.F., Briandet, R., Cerca, N., Coenye, T., Costa, A.R., Desvaux, M., Di Bonaventura, G., Hébraud, M., Jaglic, Z., Kačániová, M., Knøchel, S., Lourenço, A., Mergulhão, F., Meyer, R.L., Nychas, G., Simões, M., Tresse, O., Sternberg, C., 2017. Critical review on biofilm methods. Crit. Rev. Microbiol. 43, 313–351. https://doi.org/10.1080/1040841X.2016.1208146.

Bai, X., Dinkla, I.J.T., Muyzer, G., 2023. Shedding light on the total and active core microbiomes in slow sand filters for drinking water production. Water Res. 243, 120404. https://doi.org/10.1016/J.WATRES.2023.120404.

Balcaen, T., Vangrunderbeeck, S., De Borggraeve, W.M., Kerckhofs, G., 2025. Contrast-enhancing staining agents for ex vivo contrast-enhanced computed tomography: a review. Tomogr. Mater. Struct. 7, 100052. https://doi.org/10.1016/j.tmater.2025.100052.

Balint, R., Lowe, T., Shearer, T., 2016. Optimal contrast agent staining of ligaments and tendons for X-ray computed tomography. PLoS. One 11, e0153552. https://doi.org/10.1371/journal.pone.0153552.

Bar-On, Y.M., Phillips, R., Milo, R., 2018. The biomass distribution on Earth. Proc. Natl. Acad. Sci. 115, 6506–6511. https://doi.org/10.1073/pnas.1711842115.

Baveye, P., Vandevivere, P., Hoyle, B.L., DeLeo, P.C., de Lozada, D.S., 1998. Environmental impact and mechanisms of the biological clogging of saturated soils and aquifer materials. Crit. Rev. Environ. Sci. Technol. 28, 123–191. https://doi.org/10.1080/10643389891254197.

Bultreys, T., Boone, M.A., Boone, M.N., De Schryver, T., Masschaele, B., Van Hoorebeke, L., Cnudde, V., 2016. Fast laboratory-based micro-computed tomography for pore-scale research: illustrative experiments and perspectives on the future. Adv. Water Resour. 95, 341–351. https://doi.org/10.1016/J.ADVWATRES.2015.05.012.

Caizán-Juanarena, L., Krug, J.R., Vergeldt, F.J., Kleijn, J.M., Velders, A.H., Van As, H., Ter Heijne, A., 2019. 3D biofilm visualization and quantification on granular bioanodes with magnetic resonance imaging. Water Res. 167, 115059. https://doi.org/10.1016/j.watres.2019.115059.

Carrel, M., Beltran, M.A., Morales, V.L., Derlon, N., Morgenroth, E., Kaufmann, R., Holzner, M., 2017. Biofilm imaging in porous media by laboratory X-ray tomography: combining a non-destructive contrast agent with propagation-based phase-contrast imaging tools. PLoS. One 12, e0180374. https://doi.org/10.1371/journal.pone.0180374.

Carrel, M., Morales, V.L., Beltran, M.A., Derlon, N., Kaufmann, R., Morgenroth, E., Holzner, M., 2018. Biofilms in 3D porous media: delineating the influence of the pore network geometry, flow and mass transfer on biofilm development. Water Res. 134, 280–291. https://doi.org/10.1016/j.watres.2018.01.059.

Cnudde, V., Boone, M.N., 2013. High-resolution X-ray computed tomography in geosciences: a review of the current technology and applications. Earth. Sci. Rev. 123, 1–17. https://doi.org/10.1016/j.earscirev.2013.04.003.

Coombs, P., Wagner, D., Bateman, K., Harrison, H., Milodowski, A.E., Noy, D., West, J. M., 2010. The role of biofilms in subsurface transport processes. Q. J. Eng. Geol. Hydrogeo 43, 131–139. https://doi.org/10.1144/1470-9236/08-029.

Davit, Y., Iltis, G., Debenest, G., Veran-Tissoires, S., Wildenschild, D., Gerino, M., Quintard, M., 2011. Imaging biofilm in porous media using X-ray computed microtomography. J. Microsc. 242, 15–25. https://doi.org/10.1111/j.1365-2818.2010.03432.x.

Dawood, Y., Hagoort, J., Siadari, B.A., Ruijter, J.M., Gunst, Q.D., Lobe, N.H.J., Strijkers, G.J., de Bakker, B.S., van den Hoff, M.J.B., 2021. Reducing soft-tissue shrinkage artefacts caused by staining with Lugol's solution. Sci. Rep. 11, 19781. https://doi.org/10.1038/s41598-021-99202-2.

de Bournonville, S., Vangrunderbeeck, S., Kerckhofs, G., 2019. Contrast-enhanced MicroCT for virtual 3D anatomical pathology of biological tissues: a literature review. Contrast. Media Mol. ImAging 2019, 1–9. https://doi.org/10.1155/2019/8617406.

de Bournonville, S., Vangrunderbeeck, S., Ly, H.G.T., Geeroms, C., De Borggraeve, W.M., Parac-Vogt, T.N., Kerckhofs, G., 2020. Exploring polyoxometalates as non-destructive staining agents for contrast-enhanced microfocus computed tomography of biological tissues. Acta Biomater. 105, 253–262. https://doi.org/10.1016/j.actbio.2020.01.038.

De Muynck, W., De Belie, N., Verstraete, W., 2010. Microbial carbonate precipitation in construction materials: a review. Ecol Eng 36, 118–136. https://doi.org/10.1016/j.ecoleng.2009.02.006.

di Biase, A., Kowalski, M.S., Devlin, T.R., Oleszkiewicz, J.A., 2019. Moving bed biofilm reactor technology in municipal wastewater treatment: a review. J. Environ. Manage. 247, 849–866. https://doi.org/10.1016/j.jenvman.2019.06.053.

Dullemont, Y.J., Schijven, J.F., Hijnen, W.A.M., Colin, M., Magic-Knezev, A., Oorthuizen, W.A., 2006. Removal of microorganisms by slow sand filtration. In: Gimbel, R., Graham, N.J.D., Collins, M.R. (Eds.), Recent Progress in Slow Sand and Alternative Biofiltration Processes. IWA Publishing, London, pp. 12–20.

Early, C.M., Morhardt, A.C., Cleland, T.P., Milensky, C.M., Kavich, G.M., James, H.F., 2020. Chemical effects of diceCT staining protocols on fluid-preserved avian specimens. PLoS. One 15, e0238783. https://doi.org/10.1371/journal.pone.0238783.

Ebigbo, A., Helmig, R., Cunningham, A.B., Class, H., Gerlach, R., 2010. Modelling biofilm growth in the presence of carbon dioxide and water flow in the subsurface. Adv. Water Resour. 33, 762–781. https://doi.org/10.1016/j.advwatres.2010.04.004.

Ehrlich, H.L., 1999. Microbes as geologic agents: their role in mineral formation. Geomicrobiol. J. 16, 135–153. https://doi.org/10.1080/014904599270659.

Fierer, N., 2017. Embracing the unknown: disentangling the complexities of the soil microbiome. Nat. Rev. Microbiol. https://doi.org/10.1038/nrmicro.2017.87.

Flemming, H.-C., Wingender, J., Szewzyk, U., Steinberg, P., Rice, S.A., Kjelleberg, S., 2016. Biofilms: an emergent form of bacterial life. Nat. Rev. Microbiol. 14, 563–575. https://doi.org/10.1038/nrmicro.2016.94.

Flemming, H.-C., Wuertz, S., 2019. Bacteria and archaea on Earth and their abundance in biofilms. Nat. Rev. Microbiol. 17, 247–260. https://doi.org/10.1038/s41579-019-0158-9.

Gignac, P.M., Kley, N.J., 2014. Iodine-enhanced micro-CT imaging: methodological refinements for the study of the soft-tissue anatomy of post-embryonic vertebrates. J. Exp. Zool. B Mol. Dev. Evol. 322, 166–176. https://doi.org/10.1002/JEZ.B.22561;JOURNAL:JOURNAL:15525015.

Ginsberg, A.P., 1990. Inorganic Syntheses, Inorganic Syntheses. Wiley, Hoboken, NJ, USA. https://doi.org/10.1002/9780470132586.
Haig, S.J., Quince, C., Davies, R.L., Dorea, C.C., Collins, G., 2014. Replicating the microbial community and water quality performance of full-scale slow sand filters in laboratory-scale filters. Water Res. 61, 141–151. https://doi.org/10.1016/J.WATRES.2014.05.008.
Hassanpourfard, M., Ghosh, R., Thundat, T., Kumar, A., 2016. Dynamics of bacterial streamers induced clogging in microfluidic devices. Lab. Chip. 16, 4091–4096. https://doi.org/10.1039/C6LC01055E.
Iltis, G.C., Armstrong, R.T., Jansik, D.P., Wood, B.D., Wildenschild, D., 2011. Imaging biofilm architecture within porous media using synchrotron-based X-ray computed microtomography. Water Resour. Res. 47. https://doi.org/10.1029/2010WR009410.
Ivankovic, T., Rolland du Roscoat, S., Geindreau, C., Séchet, P., Huang, Z., Martins, J.M.F., 2016. Development and evaluation of an experimental protocol for 3-D visualization and characterization of the structure of bacterial biofilms in porous media using laboratory X-ray tomography. Biofouling 32, 1235–1244. https://doi.org/10.1080/08927014.2016.1249865.
Jeffery, N.S., Stephenson, R.S., Gallagher, J.A., Jarvis, J.C., Cox, P.G., 2011. Micro-computed tomography with iodine staining resolves the arrangement of muscle fibres. J. Biomech. 44, 189–192. https://doi.org/10.1016/j.jbiomech.2010.08.027.
Kalin, R., 2004. Engineered passive bioreactive barriers: risk-managing the legacy of industrial soil and groundwater pollution. Curr. Opin. Microbiol. 7, 227–238. https://doi.org/10.1016/j.mib.2004.04.014.
Karimi, M., Mahmoodi, M., Niazi, A., Al-Wahaibi, Y., Ayatollahi, S., 2012. Investigating wettability alteration during MEOR process, a micro/macro scale analysis. Colloids. Surf. B Biointerfaces. 95, 129–136. https://doi.org/10.1016/j.colsurfb.2012.02.035.
Karimifard, S., Li, X., Elowsky, C., Li, Y., 2021. Modeling the impact of evolving biofilms on flow in porous media inside a microfluidic channel. Water Res. 188, 116536. https://doi.org/10.1016/j.watres.2020.116536.
Kato, C.N., Shinohara, A., Hayashi, K., Nomiya, K., 2006. Syntheses and X-ray crystal structures of zirconium(IV) and hafnium(IV) complexes containing monovacant Wells−Dawson and Keggin polyoxotungstates. Inorg. Chem. 45, 8108–8119. https://doi.org/10.1021/ic060656e.
Konhauser, K.O., 2007. Introduction to Geomicrobiology. Wiley-Blackwell.
Maes, A., Pestiaux, C., Marino, A., Balcaen, T., Leyssens, L., Vangrunderbeeck, S., Pyka, G., De Borggraeve, W.M., Bertrand, L., Beauloye, C., Horman, S., Wevers, M., Kerckhofs, G., 2022. Cryogenic contrast-enhanced microCT enables nondestructive 3D quantitative histopathology of soft biological tissues. Nat. Commun. 13, 6207. https://doi.org/10.1038/s41467-022-34048-4.
Maiyo, J.K., Dasika, S., Jafvert, C.T., 2023. Slow sand Filters for the 21st century: a review. Int. J. Environ. Res. Public Health 20, 1019. https://doi.org/10.3390/ijerph20021019.
Meckenstock, R.U., Elsner, M., Griebler, C., Lueders, T., Stumpp, C., Aamand, J., Agathos, S.N., Albrechtsen, H.-J., Bastiaens, L., Bjerg, P.L., Boon, N., Dejonghe, W., Huang, W.E., Schmidt, S.I., Smolders, E., Sørensen, S.R., Springael, D., van Breukelen, B.M., 2015. Biodegradation: updating the concepts of control for microbial cleanup in contaminated aquifers. Environ. Sci. Technol. 49, 7073–7081. https://doi.org/10.1021/acs.est.5b00715.
Miller, A., Kruichak, J., Mills, M., Wang, Y., 2015. Iodide uptake by negatively charged clay interlayers? J. Environ. Radioact. 147, 108–114. https://doi.org/10.1016/J.JENVRAD.2015.05.024.
Miller, A.Z., Sanmartín, P., Pereira-Pardo, L., Dionísio, A., Saiz-Jimenez, C., Macedo, M.F., Prieto, B., 2012. Bioreceptivity of building stones: a review. Sci. Total Environ. 426, 1–12. https://doi.org/10.1016/j.scitotenv.2012.03.026.
Moulay, S., 2013. Molecular iodine/polymer complexes. J. Polym. Eng. 33, 389–443. https://doi.org/10.1515/polyeng-2012-0122.
Palumbo, G., Zullo, F., 1987. The use of iodine staining for the quantitative analysis of lipids separated by thin layer chromatography. Lipids 22, 201–205. https://doi.org/10.1007/BF02537303.
Pedley, S., Howard, G., 1997. The public health implications of microbiological contamination of groundwater. Q. J. Eng. Geol. 30, 179–188. https://doi.org/10.1144/GSL.QJEGH.1997.030.P2.10.
Pelling, H., Nzakizwanayo, J., Milo, S., Denham, E.L., MacFarlane, W.M., Bock, L.J., Sutton, J.M., Jones, B.V., 2019. Bacterial biofilm formation on indwelling urethral catheters. Lett. Appl. Microbiol. 68, 277–293. https://doi.org/10.1111/LAM.13144.
Pintelon, T.R.R., Graf von der Schulenburg, D.A., Johns, M.L., 2009. Towards optimum permeability reduction in porous media using biofilm growth simulations. Biotechnol. Bioeng. 103, 767–779. https://doi.org/10.1002/bit.22303.
Qin, C.Z., Hassanizadeh, S.M., 2015. Pore-network modeling of solute transport and biofilm growth in porous Media. Transp. Porous. Media 110, 345–367. https://doi.org/10.1007/s11242-015-0546-1.
Rolland du Roscoat, S., Martins, J.M.F., Séchet, P., Vince, E., Latil, P., Geindreau, C., 2014. Application of synchrotron X-ray microtomography for visualizing bacterial biofilms 3D microstructure in porous media. Biotechnol. Bioeng. 111, 1265–1271. https://doi.org/10.1002/bit.25168.
Salazar Marcano, D.E., Savić, N.D., Abdelhameed, S.A.M., de Azambuja, F., Parac-Vogt, T.N., 2023. Exploring the reactivity of polyoxometalates toward proteins: from interactions to mechanistic insights. JACS. Au 3, 978–990. https://doi.org/10.1021/jacsau.3c00011.
Samari-Kermani, M., de Vries, E.T., Schijven, J.F., Raoof, A., 2024. A closer look at the role of biofilms in water filtration: bridging microscopic insights with system performance. J. Water Process. Eng. 67, 106104. https://doi.org/10.1016/j.jwpe.2024.106104.
Schröer, L., Balcaen, T., Folens, K., Boon, N., De Kock, T., Kerckhofs, G., Cnudde, V., 2024. 3D Visualization of cyanobacterial biofilms using micro-computed tomography with contrast-enhancing staining agents. Tomogr. Mater. Struct., 100024 https://doi.org/10.1016/j.tmater.2024.100024.
Schröer, L., Boon, N., De Kock, T., Cnudde, V., 2021. The capabilities of bacteria and archaea to alter natural building stones – A review. Int. Biodeterior. Biodegradation. 165, 105329. https://doi.org/10.1016/j.ibiod.2021.105329.
Schröer, L., De Kock, T., Cnudde, V., Boon, N., 2020. Differential colonization of microbial communities inhabiting Lede stone in the urban and rural environment. Sci. Total Environ. 733, 139339. https://doi.org/10.1016/j.scitotenv.2020.139339.
Schröer, L., De Kock, T., Godts, S., Boon, N., Cnudde, V., 2022a. The effects of cyanobacterial biofilms on water transport and retention of natural building stones. Earth. Surf. Process. Landf. 47, 1921–1936. https://doi.org/10.1002/esp.5355.
Schröer, L., Fiers, G., Deprez, M., Boon, N., Cnudde, V., Soens, L., De Kock, T., 2022b. Examining the potential of enzyme-based detergents to remove biofouling from limestone heritage. Coatings 12, 375. https://doi.org/10.3390/COATINGS12030375.
Schulz, R., Knabner, P., 2017. Derivation and analysis of an effective model for biofilm growth in evolving porous media. Math. Methods Appl. Sci. 40, 2930–2948. https://doi.org/10.1002/mma.4211.
Singh, R., Sivaguru, M., Fried, G.A., Fouke, B.W., Sanford, R.A., Carrera, M., Werth, C.J., 2017. Real rock-microfluidic flow cell: a test bed for real-time in situ analysis of flow, transport, and reaction in a subsurface reactive transport environment. J. Contam. Hydrol. 204, 28–39. https://doi.org/10.1016/j.jconhyd.2017.08.001.
Tang, P., Xu, H., Zhang, W., Zhu, Y., Yang, J., Zhou, Y., 2023. Fluid transport in porous media based on differences in filter media morphology and biofilm growth in bioreactors. Environ. Res. 219, 115122. https://doi.org/10.1016/j.envres.2022.115122.
Vandevivere, P., Baveye, P., 1992. Saturated hydraulic conductivity reduction caused by aerobic bacteria in sand columns. Soil Sci. Soc. Am. J. 56, 1–13. https://doi.org/10.2136/sssaj1992.03615995005600010001x.
Verma, S., Kuila, A., Jacob, S., 2023. Role of biofilms in waste water treatment. Appl. Biochem. Biotechnol. 195, 5618–5642. https://doi.org/10.1007/s12010-022-04163-5.
Vickerton, P., Jarvis, J., Jeffery, N., 2013. Concentration-dependent specimen shrinkage in iodine-enhanced micro microCT. J. Anat. 223, 185–193. https://doi.org/10.1111/joa.12068.
Wagner, M., Horn, H., 2017. Optical coherence tomography in biofilm research: a comprehensive review. Biotechnol. Bioeng. 114, 1386–1402. https://doi.org/10.1002/bit.26283.
Walker, S.L., Redman, J.A., Elimelech, M., 2004. Role of cell surface lipopolysaccharides in Escherichia coli K12 adhesion and transport. Langmuir 20, 7736–7746. https://doi.org/10.1021/la049511f.
Wilking, J.N., Zaburdaev, V., De Volder, M., Losick, R., Brenner, M.P., Weitz, D.A., 2013. Liquid transport facilitated by channels in Bacillus subtilis biofilms. Proc. Natl. Acad. Sci. 110, 848–852. https://doi.org/10.1073/pnas.1216376110.
Withers, P.J., Bouman, C., Carmignato, S., Cnudde, V., Grimaldi, D., Hagen, C.K., Maire, E., Manley, M., Du Plessis, A., Stock, S.R., 2021. X-ray computed tomography. Nat. Rev. Methods Primers 1, 18. https://doi.org/10.1038/s43586-021-00015-4.
Woodard, H.Q., White, D.R., 1986. The composition of body tissues. Br. J. Radiol. 59, 1209–1218. https://doi.org/10.1259/0007-1285-59-708-1209.
Zhang, N., Thompson, C.E.L., Townend, I.H., Rankin, K.E., Paterson, D.M., Manning, A.J., 2018. Nondestructive 3D imaging and quantification of hydrated biofilm-sediment aggregates using X-ray microcomputed tomography. https://doi.org/10.1021/acs.est.8b03997.